

Faceting, composition and crystal phase evolution in III–V antimonide nanowire heterostructures revealed by combining microscopy techniques

This article has been downloaded from IOPscience. Please scroll down to see the full text article.

2012 Nanotechnology 23 095702

(<http://iopscience.iop.org/0957-4484/23/9/095702>)

View [the table of contents for this issue](#), or go to the [journal homepage](#) for more

Download details:

IP Address: 131.155.108.10

The article was downloaded on 15/02/2012 at 09:48

Please note that [terms and conditions apply](#).

# Faceting, composition and crystal phase evolution in III–V antimonide nanowire heterostructures revealed by combining microscopy techniques

Tao Xu<sup>1</sup>, Kimberly A Dick<sup>2,3</sup>, Sébastien Plissard<sup>1,4</sup>, Thanh Hai Nguyen<sup>1</sup>,  
Younes Makoudi<sup>1</sup>, Maxime Berthe<sup>1</sup>, Jean-Philippe Nys<sup>1</sup>, Xavier Wallart<sup>1</sup>,  
Bruno Grandidier<sup>1</sup> and Philippe Caroff<sup>1</sup>

<sup>1</sup> Institut d'Electronique, de Microélectronique et de Nanotechnologie, UMR CNRS 8520, Avenue Poincaré, BP 60069, 59652 Villeneuve d'Ascq, France

<sup>2</sup> Solid State Physics, Lund University, Box 118, S-221 00 Lund, Sweden

<sup>3</sup> Polymer & Materials Chemistry, Lund University, Box 124, S-221 00 Lund, Sweden

<sup>4</sup> Eindhoven University of Technology, NL-5600 MB Eindhoven, The Netherlands

E-mail: [Bruno.Grandidier@isen.univ-lille1.fr](mailto: Bruno.Grandidier@isen.univ-lille1.fr) and [Philippe.Caroff@iemn.univ-lille1.fr](mailto: Philippe.Caroff@iemn.univ-lille1.fr)

Received 18 October 2011, in final form 17 December 2011

Published 6 February 2012

Online at [stacks.iop.org/Nano/23/095702](http://stacks.iop.org/Nano/23/095702)

## Abstract

III–V antimonide nanowires are among the most interesting semiconductors for transport physics, nanoelectronics and long-wavelength optoelectronic devices due to their optimal material properties. In order to investigate their complex crystal structure evolution, faceting and composition, we report a combined scanning electron microscopy (SEM), transmission electron microscopy (TEM), and scanning tunneling microscopy (STM) study of gold-nucleated ternary InAs/InAs<sub>1-x</sub>Sb<sub>x</sub> nanowire heterostructures grown by molecular beam epitaxy. SEM showed the general morphology and faceting, TEM revealed the internal crystal structure and ternary compositions, while STM was successfully applied to characterize the oxide-free nanowire sidewalls, in terms of nanofaceting morphology, atomic structure and surface composition. The complementary use of these techniques allows for correlation of the morphological and structural properties of the nanowires with the amount of Sb incorporated during growth. The addition of even a minute amount of Sb to InAs changes the crystal structure from perfect wurtzite to perfect zinc blende, via intermediate stacking fault and pseudo-periodic twinning regimes. Moreover, the addition of Sb during the axial growth of InAs/InAs<sub>1-x</sub>Sb<sub>x</sub> heterostructure nanowires causes a significant conformal lateral overgrowth on both segments, leading to the spontaneous formation of a core–shell structure, with an Sb-rich shell.

 Online supplementary data available from [stacks.iop.org/Nano/23/095702/mmedia](http://stacks.iop.org/Nano/23/095702/mmedia)

(Some figures may appear in colour only in the online journal)

## 1. Introduction

Progress in control over bottom-up epitaxial growth of III–V nanowires has rendered them one of the most interesting nanotechnology building blocks for optics, electronics, energy

and biosensing applications, because of their high level of tunability in terms of alloy formation and heterostructure engineering. Although a good control has been gained over the dimensions, size dispersions and positioning of these nanowires, challenges remain in understanding their crystal

structure changes, surface properties and the incorporation of impurities. Polytypism, stacking faults and twin defects can easily occur in an uncontrolled way in nanowires growing along the  $\langle 111 \rangle$  direction [1], which dramatically affect the electronic and optical properties [2, 3]. Recently, it has become clear that crystal phase engineering in nanowires presents unique opportunities to observe novel fundamental properties, such as in twinning or polytypic superlattices [4–8]. These structural changes are often coupled to a change of surface orientations [9, 10]. Moreover, an understanding of the surface structure is of particular importance for nanowire applications, since it is well understood that the electrical, optical, thermal and mechanical properties are typically dominated by the nanowire surfaces [11–16].

Among the existing semiconductor nanowire materials, antimonides are emerging as a particularly important class due to properties such as high carrier mobilities and narrow direct band gaps. Ternary Sb-based materials such as  $\text{InAs}_{1-x}\text{Sb}_x$  also exhibit bandgaps tunable through an important part of the infrared spectrum, and are thus of interest for infrared emission and detection applications. Reports of antimonide nanowire growth [9, 17–23] indicate that these materials can behave differently from conventional arsenide and phosphide nanowires, with lower growth rates, different group III element incorporation into the alloy seed particle and different facet structures. Intriguingly, binary antimonide nanowires generally do not show the polytypism typical of other III–V nanowire materials, instead exhibiting pure ZB phase over a large range of growth conditions. The same effect is reported for ternary antimonide nanowires, including  $\text{GaAs}_{1-x}\text{Sb}_x$  grown by molecular beam epitaxy (MBE) [24, 25], and  $\text{InAs}_{1-x}\text{Sb}_x$  nanowires grown by metalorganic vapor phase epitaxy (MOVPE) [26]: for the entire range of Sb concentrations investigated in these works, the nanowire crystal structure is observed to be ZB. This is in contrast to  $\text{Ga}_{1-x}\text{In}_x\text{As}$  nanowires which can show crystal structure and defect density variations as a function of their composition [27]. It has also been suggested that Sb could change the crystal structure of InAs nanowires from WZ to ZB in a transition from InAs to InSb [17], even though any Sb present in the InAs was below detection limits.

It has similarly been reported that impurities such as dopants can play a crucial role in determining the crystal structure of III–V nanowires, and that the incorporation of even a small concentration of dopant atoms can lead to dramatic structural changes. For example, zinc (p-type) changes the crystal structure of InP and GaP from wurtzite (WZ) to periodically twinned zinc blende (ZB) [28, 29]. Also, selenium (n-type) changes InAs nanowires from pure WZ to defect-free pure ZB [11]. These observations are of special importance because the use of impurities such as dopants or surfactants is necessary to achieve advanced nanowire devices [30].

In order to understand and control the structural changes induced by trace atoms, it is necessary to be able to detect them both in bulk and at the surfaces. A few techniques are becoming available which can give precise

information at an atomic level, such as high resolution Cs-corrected transmission electron microscopy (TEM) and laser assisted atom probe tomography (LA-APT). However, these techniques only give reliable statistical counts of the impurity distribution and concentration in the bulk, and not at or in the vicinity of the surface [31, 32]. Alternatively, scanning tunneling microscopy (STM) is a technique of choice to access quantitative information, down to atomic resolution and single atom precision, at or close to the surface [33]. In III–V nanowires, however, only very few reports exist of scanning tunneling microscopy studies of internal structure [34, 35], and even fewer studies exist for the characterization of the nanowire surfaces [36]. In the latter case, this arises mainly due to experimental difficulties associated with the removal of the native oxide and the non-planar geometry of nanowires. Surface structural investigation requires complex preparation protocols (annealing, atomic hydrogen etching and eventually group V overpressure), especially since III–V compound semiconductors have a low congruent evaporation temperature. Moreover, post-growth oxide removal procedures damage the surface [36], precluding direct access to the originally grown oxide-free surface.

In this work we investigate the effect of composition on the surface facets and crystal structure of ternary  $\text{InAs}_{1-x}\text{Sb}_x$  nanowires and  $\text{InAs}/\text{InAs}_{1-x}\text{Sb}_x$  heterostructures grown by MBE, using a combination of SEM, high resolution TEM and STM. For the latter we demonstrate the development of an *in situ* As capping technique to prevent oxidation in ambient air and to thus give access to surface facets, free of native oxide (see supplementary figure S5 available at [stacks.iop.org/Nano/23/095702/mmedia](http://stacks.iop.org/Nano/23/095702/mmedia)). From the complementary analysis performed with different microscopy techniques as well as x-ray energy-dispersive spectroscopy (XEDS) as a function of the Sb content, we show that the addition of a very small amount of Sb to InAs nanowires leads to a perfectly tunable change of the crystal structure from pure WZ to pure ZB via intermediate stacking fault and pseudo-periodic twinning regimes. This structural evolution is associated with a complex core–shell morphological transformation, providing a perfect test bed for local surface analysis techniques, since quantitative compositional information can be gained from the differently oriented sidewalls of the nanowires.

## 2. Methods

### 2.1. Nanowire growth

All the samples were grown by gas source MBE on top of a short InP nanowire stem on InP(111)B substrates. The use of a short InP nanowire stem shifts the nucleation interface from wire–substrate to wire–wire. The substrate native oxide was first removed in a 5% hydrofluoric acid solution, prior to electron beam assisted evaporation of a thin gold film (nominally 3 Å), performed *ex situ* at a low deposition rate. The substrates were then introduced into the reactor. Gold droplets self-formed during the annealing and deoxidation step at 525 °C under  $\text{P}_2$  flux, by dewetting of the gold film. V/III ratios were calculated from 2D equivalent growth

rates, calibrated by reflection high energy electron diffraction (RHEED) and set to 2.0–2.2 for InP and InAs, using an indium flux equivalent to  $0.5 \text{ ML s}^{-1}$  in a 2D growth regime. InP stem growth was initiated at  $410^\circ\text{C}$ , and InAs nanowires were subsequently grown by a direct switch from  $\text{P}_2$  to  $\text{As}_2$  molecular fluxes. The growth times were set to 15 min and 23–25 min for InP and InAs respectively. The final top  $\text{InAs}_{1-x}\text{Sb}_x$  segment was finally grown sequentially by directly switching on the  $\text{Sb}_2$  flux for 9–20 min depending on the sample. A Veeco valved cracker antimony cell was set at evaporator and cracker temperatures of  $500^\circ\text{C}$  and  $900^\circ\text{C}$  respectively. The antimony fraction was controlled by valve opening, measured by flux gauge, and precisely calibrated over the full range using induced group V limited RHEED oscillations [37] during homoepitaxial GaSb layer-by-layer growth. The  $\text{Sb}_2$  flux was measured between  $1 \times 10^{-8}$  Torr ( $\text{InAs}_{1-x}\text{Sb}_x$ ,  $x < 0.02$ ) and  $2 \times 10^{-6}$  Torr ( $\text{InSb}$ , V/III = 3.0), and the group V equivalent incorporation rate was evaluated respectively, between  $0.02 \text{ ML s}^{-1}$  and  $1.5 \text{ ML s}^{-1}$ . Each of the antimony fractions  $x$  in the  $\text{InAs}_{1-x}\text{Sb}_x$  ( $x$  between 0 and 1.0) was evaluated by XEDS point-scan analysis.

## 2.2. Scanning and transmission microscopy

Morphological evaluations were performed using field emission scanning electron microscopes (SEM) (Zeiss Ultra 55, Zeiss Supra 55) operated at 10–15 kV. High resolution transmission electron microscopy (HRTEM) was used to investigate the crystal structure of the samples with increasing fraction of Sb. The HRTEM images were acquired with a 300 kV field emission gun TEM (JEM 3000F) with a point resolution of  $1.6 \text{ \AA}$ . The images were recorded along the  $(1\bar{1}0)$  zone axis, to allow the detection of stacking defects and change of crystal structure in the cubic cell, using a  $2k \times 2k$  CCD camera. Samples for HRTEM were obtained by depositing nanowires onto carbon film coated Cu grids, by gently rubbing the grid against the sample, in most cases breaking the nanowires off at the base. X-ray energy-dispersive spectroscopy (XEDS) analysis operated in the high-angle annular dark field scanning TEM (HAADF-STEM) mode (point resolution  $1.2 \text{ \AA}$ ) was performed on all the nanowires to investigate the chemical composition using point analysis with a probe size  $0.6 \text{ nm}$ . The nominal compositional resolution for these conditions should be of the order of 1 wt% or better. However the partial overlap of In and Sb L peaks complicates the quantification, particularly for low Sb. We therefore estimate the error in the quantification of  $\text{InAs}_{1-x}\text{Sb}_x$  nanowires at about 4%. The spatial resolution for this accelerating voltage, material and thickness is about  $3 \text{ nm}$ .

## 2.3. Sample preparation for STM study

For the STM characterizations, at the end of the growth, the samples were capped with a thin layer of As, deposited at room temperature for 30–50 min (depending on the sample), under high  $\text{As}_2$  flux, transferred to air and, finally, loaded into an ultra-high vacuum (UHV) system that contains

a low temperature scanning tunneling microscope. The evaporation of the capping layer was achieved at  $350^\circ\text{C}$  for 4 h, monitoring the As desorption with mass spectrometry. The main steps are illustrated in supplementary figure S5 (available at [stacks.iop.org/Nano/23/095702/mmedia](http://stacks.iop.org/Nano/23/095702/mmedia)). A low evaporation temperature of the amorphous As layer ensures that the nanowires characterized by STM keep their structural and chemical properties unchanged with respect to the as-grown nanowires. The morphologies of the annealed and as-grown nanowires were compared with those observed by SEM. The comparison showed no significant modification of the overall morphology. The As decapping procedure was optimized in terms of both annealing temperature and duration to minimize potential gold diffusion on the sidewalls. Note that in the STM image in supplementary figure S9 (available at [stacks.iop.org/Nano/23/095702/mmedia](http://stacks.iop.org/Nano/23/095702/mmedia)), several nm-sized protrusions can be seen (arrows) and are associated with Au-rich clusters, which was confirmed by XEDS.

In order to image the nanowires with STM, the nanowires were subsequently cleaved by manipulating the sample into direct contact with another substrate, where the nanowires fall down flat on the surface of a fresh Si (111)-(7 × 7) surface, prepared by standard procedures [38, 39]. Three types of nanowires were investigated with STM: pure InAs nanowires (reference), nanowires with an intended low concentration of Sb ( $x = 0.05$ ) and nanowires where the concentration of Sb was nominally doubled. All the STM observations were performed at  $77 \text{ K}$ .

## 3. Results and discussion

### 3.1. Crystal structure and composition

Figure 1 illustrates the crystal structure evolution of the  $\text{InAs}_{1-x}\text{Sb}_x$  segment with composition. Since the seed particle diameter can strongly influence the crystal structure [2], only nanowires with a selected diameter of 40–50 nm (measured at the tip) are presented in this study, to remove the parasitic influence of this parameter. Additional TEM images are included in supplementary figure S1 (available at [stacks.iop.org/Nano/23/095702/mmedia](http://stacks.iop.org/Nano/23/095702/mmedia)) which show the tips of the nanowires, including the gold seed particle, and illustrate the various degrees of lateral overgrowth as a function of antimony fraction. We first note that pure InAs nanowires (figure 1(a)) have a nearly perfect WZ structure with fewer than 0.5 stacking faults per  $\mu\text{m}$  length for a diameter of 40 nm. This pure WZ structure is most often observed in other reports of gold-seeded InAs and GaAs nanowires grown by MBE [40–46]. By contrast, pure InSb nanowires (figure 1(b)) show a perfect ZB crystal structure without stacking defects. Additional higher and lower magnification TEM images of pure InAs and InSb nanowires are shown in supplementary figure S2 (available at [stacks.iop.org/Nano/23/095702/mmedia](http://stacks.iop.org/Nano/23/095702/mmedia)). As noted above, this observation is consistent with other reports of InSb nanowires grown by MOVPE and chemical beam epitaxy (CBE), as well as ternary  $\text{InAs}_{1-x}\text{Sb}_x$  nanowires grown by MOVPE with  $x$  higher than 0.15, as determined by XEDS [26]. In this work, the perfect

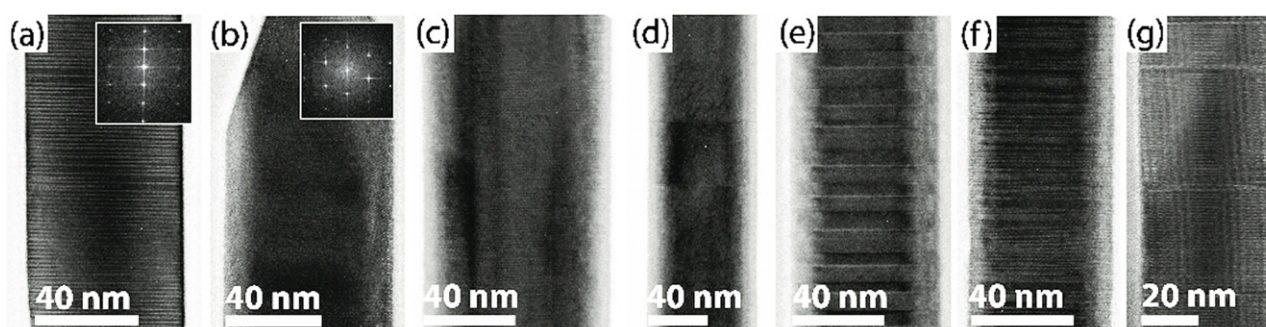


**Figure 1.** Transmission electron microscopy images, taken along the  $(1\bar{1}0)$  zone axis, of  $\text{InAs}_{1-x}\text{Sb}_x$  top segments from  $\text{InAs}/\text{InAs}_{1-x}\text{Sb}_x$  heterostructure nanowires all having similar seed particle diameters (40–50 nm): (a)  $\text{InAs}$  ( $x = 0$ ) with pure wurtzite (WZ) structure, with associated fast Fourier transform (FFT) as inset; (b)  $\text{InSb}$  ( $x = 1$ ) with pure zinc blende (ZB) structure, with FFT as inset; (c)  $x = 0.12$ , pure ZB structure; (d)  $x = 0.08$ , ZB with occasional twin planes; (e)  $x = 0.05$ , ZB with pseudo-periodic twin planes; (f)  $x \approx 0.03$ , mixed ZB and WZ with frequent stacking faults and twins; (g) Sb content below XEDS detection limits (nominal Sb flux two-thirds of (f)), WZ structure with regular stacking faults. Additional TEM images are included in supplementary figures S1–S4 (available at [stacks.iop.org/Nano/23/095702/mmedia](http://stacks.iop.org/Nano/23/095702/mmedia)).

ZB structure is maintained for 40–50 nm diameter nanowires down to an average composition of about  $x = 0.12$  (measured by XEDS point analysis at the lateral midpoint near the tip of the  $\text{InAs}_{1-x}\text{Sb}_x$  segment, to minimize the contribution from the lateral overgrowth) (figure 1(c)).

As the Sb content is reduced to about  $x = 0.08$  (figure 1(d)), we observe the appearance of occasional twin planes in the  $\text{InAs}_{1-x}\text{Sb}_x$  segment, with a density of about  $7 \mu\text{m}^{-1}$ . For an Sb fraction of about  $x = 0.05$  (figure 1(e)), the nanowires exhibit a pseudo-periodic twinning structure. Reducing the Sb fraction to an estimated  $x \approx 0.03$  yields a very mixed crystal structure with segments of both WZ and ZB, together with dense stacking faults and twins (figure 1(f)). Further reduction of the  $\text{Sb}_2$  flux by one third yields a predominantly WZ structure with a stacking fault density of about  $18 \mu\text{m}^{-1}$  (figure 1(g)), but the Sb composition in this case could not be clearly distinguished from the background by XEDS analysis ( $x \leq 0.02$ ). Higher magnification TEM images of  $\text{InAs}_{1-x}\text{Sb}_x$  nanowires, and associated fast Fourier transforms (FFTs), are shown in supplementary figures S3 and S4 (available at [stacks.iop.org/Nano/23/095702/mmedia](http://stacks.iop.org/Nano/23/095702/mmedia)) for  $x = 0.12$  to  $x \leq 0.02$ .

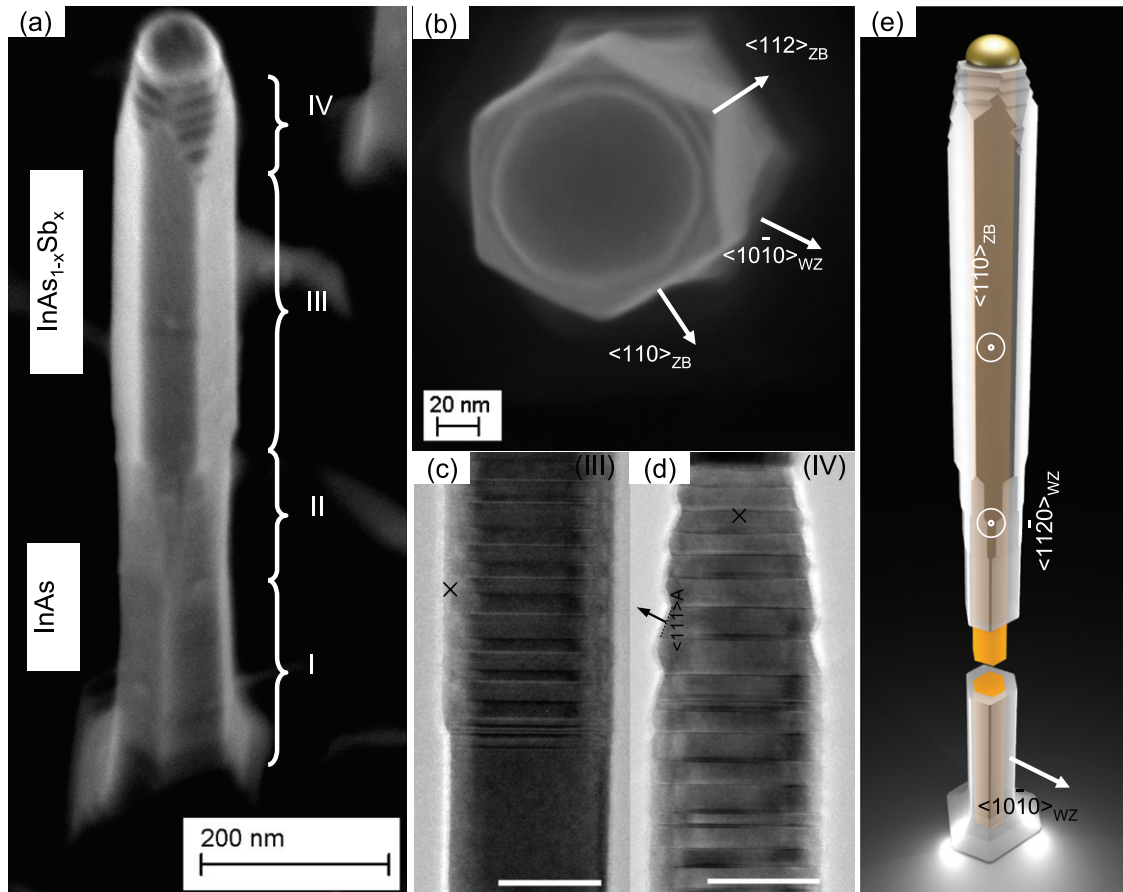
### 3.2. 3D morphology

Figure 2 illustrates the facet changes induced over the full single nanowire heterostructure by the Sb incorporation. Two nanowire segments, having similar lengths, are clearly visible along the nanowire axis. These nanowires were imaged by SEM after As decapping (see section 2.3 and supplementary figure S5 available at [stacks.iop.org/Nano/23/095702/mmedia](http://stacks.iop.org/Nano/23/095702/mmedia)). The bottom part is nominally  $\text{InAs}$  and the top part  $\text{InAs}_{1-x}\text{Sb}_x$  with  $x$  of about 0.05. This composition corresponds to figure 1(e), and was selected as a midpoint in the structural evolution in order to best illustrate the corresponding facet evolution. The morphological changes are described following the nanowire from bottom to top, and designated using a numbering system in figure 2 from I to IV. First, it is clear by comparison with the diameter of

the top seed particle in figures 2(a) and (b) that the entire structure exhibits lateral overgrowth. HRTEM investigation reveals that, as expected, the bottom segment is purely WZ while the entire nominal  $\text{InAs}_{1-x}\text{Sb}_x$  segment exhibits periodic twin planes, as visible in figures 2(c) and (d). The interface between the bottom WZ  $\text{InAs}$  segment and the upper  $\text{InAs}_{1-x}\text{Sb}_x$  segment is clearly seen in figure 2(c); further investigation of the double heterostructures indicates that this interface is typically atomically sharp, while the reverse interface (back to  $\text{InAs}$ ) may have a single defect plane (see supplementary figure S7 available at [stacks.iop.org/Nano/23/095702/mmedia](http://stacks.iop.org/Nano/23/095702/mmedia)).

Returning to the facet structure seen in figure 2(a), we find that the bottom segment (I) consists of  $\{10\bar{1}0\}$  facets, similar to what is observed in pure  $\text{InAs}$  nanowires of WZ crystal structure. In II, twelve facets can be recognized, and are due to overgrowth favoring the formation of  $\{11\bar{2}0\}$  facets, that alternate with wider  $\{10\bar{1}0\}$  sidewalls. Plante *et al* have reported a similar observation for  $\text{GaAs}$  nanowires, where the facets evolved from  $\{1100\}$  to  $\{2\bar{1}10\}$  due to self-overgrowth after extended growth time [47]. This indicates that Sb-induced lateral growth enhancement is not fundamentally different from homoepitaxial overgrowth. Moreover, the absence of the six  $\{11\bar{2}0\}$  facets at the bottom of the  $\text{InAs}$  segment can now be understood as due to reduced overgrowth, resulting from a competition for the incorporation of mobile adatoms between planar parasitic growth and the nanowire radial growth.

The area denoted as III starts when Sb is switched on during growth, leading to a change of crystal phase from WZ to ZB. Six  $\{110\}$  flat facets are observed. The observation of these facets is nearly always associated with pure, untwinned ZB nanowires [48]. Indeed, the difference in faceting between the WZ and ZB segments is even more clearly observed in multiple heterostructure nanowires as in supplementary figure S7 (available at [stacks.iop.org/Nano/23/095702/mmedia](http://stacks.iop.org/Nano/23/095702/mmedia)). However, it is clear from the TEM images in figure 2 that the internal structure of this nanowire in region III consists of a pseudo-periodic twinned ZB



**Figure 2.** SEM images of InAs/InAs<sub>1-x</sub>Sb<sub>x</sub> nanowire heterostructure in tilted view (a) and top view (b), with  $x = 0.05$  measured just below the seed particle (indicated by the cross position in (d)), illustrating a complex faceting that changes along the nanowire axis, as marked in (a) from I to IV, and described in the text. (c), (d) Corresponding TEM images, taken along the  $\langle 1\bar{1}0 \rangle$  zone axis, of a nanowire from the same sample showing the InAs/InAs<sub>1-x</sub>Sb<sub>x</sub> interface (c) and top part (d), respectively (scale bar: 40 nm). The crosses in (c) and (d) represent the approximate regions in which XEDS point-scan analyses were performed to evaluate the Sb compositions in the shell and the core, respectively. (e) 3D model of the complete InAs/InAs<sub>1-x</sub>Sb<sub>x</sub> nanowire heterostructure, as derived from SEM and TEM observations at different viewing angles and zone axes. At the bottom, the InAs<sub>1-x</sub>Sb<sub>x</sub> shell (in gray) was extruded to reveal the wurtzite pure InAs stem (yellow). Higher magnification images and close-up views revealing the key morphological changes and faceting are shown in supplementary figure S6 (available at [stacks.iop.org/Nano/23/095702/mmedia](http://stacks.iop.org/Nano/23/095702/mmedia)).

structure. Previously observed twinning superlattices have been associated with a sawtooth facet morphology [28, 29, 49, 50]. This surprising observation of flat  $\{110\}$  sidewalls associated with periodic twinning can be understood by considering region IV in figures 2(a) and (d). Indeed, in this region, sawtooth facets are clearly visible perpendicular to equivalent  $\langle 112 \rangle$  directions; they consist of alternating  $\{111\}A$  and  $\{111\}B$  facets. It is well known that the diffusion length of the impinging adatoms adsorbed in region IV (close to the seed particle) allows for their direct incorporation into the seed particle, which favors axial growth over lateral growth [43, 44]. Therefore region IV of the nanowire has not been overgrown as much as region III. Region III is thus understood to result from a complete transformation from sawtooth morphology to flat  $\{110\}$  sidewalls. Looking at figure 2(d) in more detail reveals that the upward-facing  $\{111\}A$  facets have a larger area than the downward-facing  $\{111\}B$  facets. This is coherent with the result obtained in [51], where the  $\{111\}A$  and  $\{111\}B$  planes do not overgrow in an equivalent manner.

Overgrowth could have dramatic consequences for nanowire device performance, because of the crystal plane orientation dependence of the Fermi level pinning and the possible influence on doping incorporation. However, it can also be viewed as an advantage for studying a wealth of new nanofacets, not accessible in the 2D systems, because of the difficulty in obtaining the WZ phase. Indeed, the nanowire heterostructure system studied in this work could give access, for the first time, to all of the  $\{110\}$ ,  $\{111\}$ ,  $\{1\bar{1}00\}$  and  $\{11\bar{2}0\}$  facets in a single nanowire, as shown in the 3D model illustrating the faceting of the nanowire (figure 2(e)). As a result of the overgrowth, all the facets should be composed of a ternary InAs<sub>1-x</sub>Sb<sub>x</sub> alloy. Using STM, we therefore have access to their surface properties as a function of crystal phase (WZ and ZB).

### 3.3. Surface structure

Figure 3(a) shows a large-scale STM image of a nanowire from the same sample as the nanowires shown in figures

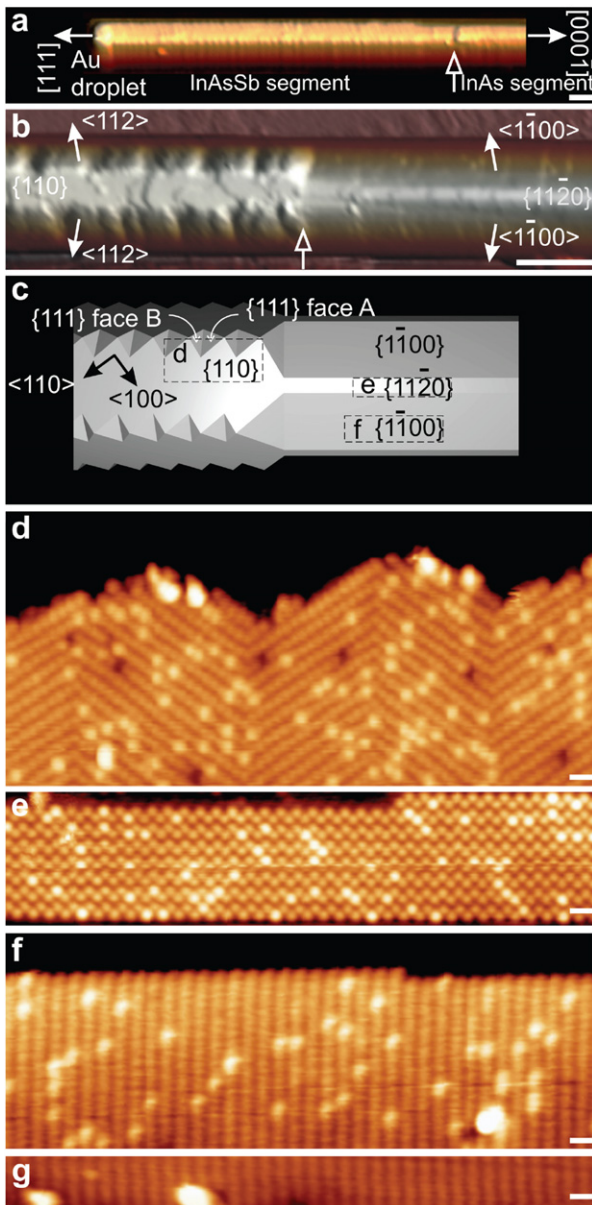


**Figure 3.** (a) Large scale three-dimensional STM image of a  $\langle 0001 \rangle / \langle \bar{1}\bar{1}\bar{1} \rangle B$ -oriented InAs/InAs $_{1-x}$ Sb $_x$  nanowire lying flat on a Si(111) surface. (b) Close-up view of the interface region between the InAs and InAs $_{1-x}$ Sb $_x$  segments. The open arrows point to the interface between the two segments, whereas the white arrow indicates the directions normal to the sidewalls. (c) 3D model close to the interface between the top and bottom segments that shows where the high resolution STM images, (d)–(f), have been recorded. Crystallographic directions of interest are indicated. (d) High resolution STM image of the {110} sidewall. (e) High resolution STM image of the {1120} sidewall. (f) High resolution STM image of the {1100} sidewall. The STM images in (d) and (f) were obtained on a nanowire with an XEDS-evaluated core concentration of Sb of  $x = 0.05$  while in (e)  $x = 0.10$ . (g) High resolution STM image of the  $\{1\bar{1}00\}$  sidewall of a pure InAs nanowire. The scale bars are 80 nm in (a) and (b) and 1 nm in (d)–(g). The STM images were acquired with a tunneling current of 10 pA and sample voltages of (a), (b)  $-3.5$  V, (c)–(f)  $-3.0$  V.

1(e) and 2 (after As decapping). The gold seed particle is clearly seen at the top of the nanowire (left part of the image), while a small constriction appears 1  $\mu\text{m}$  below this particle.

We attribute the constriction to the interface between the top InAs $_{1-x}$ Sb $_x$  segment and the bottom segment, in agreement with the TEM observation of figure 2(c). The interface is better seen in the enlarged view of figure 3(b) and corresponds to the point along the growth axis where a strong structural change of the sidewall roughness occurs. While the bottom segment facing the STM tip consists of a narrow sidewall with periodic atomic steps (seen as dark lines perpendicular to the growth direction), the InAs $_{1-x}$ Sb $_x$  segment reveals two types of alternating sidewalls: a rather flat sidewall with its normal direction perpendicular to the substrate, and a sawtooth-faceted sidewall (arrows pointing in the  $\langle 112 \rangle$  direction in figure 3(b)). On the flat sidewall, the major visible corrugation is related to the presence of atomic terraces, whereas on the adjacent sidewalls, deep trenches are observed and occur in antiphase along the growth axis. We note that the widths of the deep trenches are probably emphasized by tip artifacts, because these sidewalls are inclined with respect to the tip axis.

In order to determine the orientations of the sidewalls, high resolution STM images were acquired on the top and bottom segments of the nanowire. Figure 3(d) shows an occupied state STM image obtained on the flat sidewall of the InAs $_{1-x}$ Sb $_x$  segment, where the anion sublattice is clearly resolved. The atomic structure looks like the one that is typically observed in the (110) plane of III–V semiconductor materials with cross-sectional STM [52]. It consists of parallel atomic rows running along a  $\langle 1\bar{1}0 \rangle$  direction, making an angle of  $35.3^\circ$  with the  $\langle \bar{1}\bar{1}\bar{1} \rangle B$  growth axis. Therefore, we attribute this sidewall to a {110} plane of a ZB crystal. Interestingly, twin boundaries perpendicular to the growth direction are also observed on the {110} sidewall (see also [35]). The separation between two successive boundaries varies between 5 and 10 nm on average, in agreement with the pseudo-periodicity of the twinning superlattice seen in figures 1(e) and 2(c). This reversal in the ZB stacking sequence leads to a rotation of the crystallite by  $60^\circ$  around the growth axis. Such rotation explains why the edges of the {110} sidewalls exhibit a sawtooth shape: as the twins are formed through the whole cross-section of the nanowire, trenches build up in antiphase and account for the roughness of the adjacent sidewalls. This roughness was rarely observed by SEM inspections, because of its small dimensions (an exception is shown in supplementary figure S8 available at [stacks.iop.org/Nano/23/095702/mmedia](http://stacks.iop.org/Nano/23/095702/mmedia)), illustrating the need for complementary local probe techniques and electron microscopy. Finally, from the SEM analysis shown in figure 2(a) it is clear that these rough sidewalls are the extensions over the entire ZB segment of the alternating {111}A and {111}B facets that were only visible in region IV of figure 2(a). The STM images reveal that the {111}A facets are rather flat in contrast with the {111}B facets, in complete agreement with TEM observations (figure 2(d)).

We now turn to the bottom segment, shown by TEM characterization to have a pure WZ structure (figure 1(a)). As seen in figure 3(b) and schematically shown in (c), the large {110} sidewall from the top ZB segment extends into the bottom WZ region via a narrow  $\{11\bar{2}0\}$  sidewall, located

in between two larger  $\{1\bar{1}00\}$  sidewalls. Figure 3(e) reveals that the atomic structure of the  $\{11\bar{2}0\}$  sidewall differs from the  $\{110\}$  sidewall. It consists of zigzag chains propagating along the growth direction, consistent with the observation of Hilner *et al* [36]. This result independently confirms that the WZ structure is transferred to the overgrown  $\text{InAs}_{1-x}\text{Sb}_x$  shell up to the surface. On the adjacent  $\{1\bar{1}00\}$  sidewalls (shown by arrows on the right-hand side of figure 3(b)), the atomic rows are observed to be perpendicular to the growth direction as shown in figure 3(d), which is consistent with the atomic rows that form on a  $\{1\bar{1}00\}$  WZ sidewall [36, 52].

### 3.4. Surface and overgrowth composition

A more careful observation of the high resolution STM images for all types of sidewall reveals the presence of numerous bright protrusions with an atomic size, when the anion sublattice is imaged. In order to understand their origin, figure 3(g) shows an STM image of a  $\{1\bar{1}00\}$  sidewall obtained for a pure InAs nanowire. While a few adsorbates are seen on this sidewall, most of them clearly differ (in size and position) from the typical bright protrusions found on the nanowires terminated with an  $\text{InAs}_{1-x}\text{Sb}_x$  segment (this is more clearly shown in supplementary figure S9 available at [stacks.iop.org/Nano/23/095702/mmedia](http://stacks.iop.org/Nano/23/095702/mmedia)). In addition, we compared the number of these typical bright protrusions between images such as the ones seen in figures 3(e) and (d), which were acquired on the bottom segments of nanowires with higher and lower concentrations of Sb respectively. From this statistical analysis, we found fractions of bright atoms with respect to the total number of anions of 12.9% and 7.7%, in agreement with an increase of Sb atom concentration by a factor of two during this nanowire sample growth. Therefore, we identify the bright protrusions, which are seen on all the sidewalls when an  $\text{InAs}_{1-x}\text{Sb}_x$  segment is grown, as Sb atoms. We note that the contrast of Sb atoms in comparison with As atoms is consistent with previous cross-sectional STM studies of antimonide-based alloys [53–56]. The rather constant contrast height between all the bright atoms with respect to the As sublattice indicates that only the Sb atoms belonging to the surface layer are observed.

The presence of Sb atoms on the lower segment confirms that an  $\text{InAs}_{1-x}\text{Sb}_x$  shell is grown around the InAs core, as described above from the SEM and TEM analysis of the nanowires. The growth of a shell is further corroborated by the fact that the  $\{11\bar{2}0\}$  sidewalls are difficult to observe for the nanowires grown with the lowest concentration of Sb, these sidewalls being generally replaced by steps that have a similar appearance to the ones seen in figure 4(d) of Hilner *et al* [36]. For sufficiently high Sb concentration, the composition determined by STM can be compared with the one obtained by XEDS point analysis. Indeed, detailed XEDS studies were performed to quantify the composition just below the seed particle (typically about 50 nm from the nanowire–particle interface), where virtually no overgrowth is present (figure 2(a), zone IV), and on the sides of the top and bottom segments of the nanowire. These compositions were then compared to average values given by measurements

**Table 1.** Proportion of Sb atoms with respect to the anion sublattice measured by XEDS point mode analysis in the core and shell of  $\text{InAs}_{1-x}\text{Sb}_x$  nanowires and by STM at the surface of  $\text{InAs}_{1-x}\text{Sb}_x$  nanowires. The investigated nanowires correspond to the nanowires shown in figures 1(e), 2 and 3(a), (b), (d) and (f).

Sb composition (% of anions)	XEDS, average (lateral midpoint)	XEDS, shell	XEDS, core	STM
Top InAsSb ZB segment	9	12–13	4–5	14
Bottom InAs/InAsSb WZ segment	6	9–10	0 (assumed)	8

of the central region (where both overgrowth and core material counts are added) to confirm that measurements at the tip of the nanowire give reasonable estimates of the core composition. As shown in table 1, for  $x = 0.05$  (core composition), the quantifications of Sb atoms at the surfaces of the nanowire (measured by STM) and in the shell (measured by XEDS) are similar, suggesting that the surface composition corresponds reasonably to the bulk shell composition. Note that the measured XEDS compositions are very similar, within our detection limit, for as-grown samples and samples having undergone the complete As capping/decapping procedure, suggesting that the decapping procedure does not significantly affect the shell composition. Interestingly, we find that the proportion of Sb atoms on the surfaces of the lower segments is higher than the estimated Sb concentration in the axial  $\text{InAs}_{1-x}\text{Sb}_x$  segment (8% of anions, versus 5% measured just below the Au particle).

It is clear that the Sb incorporation into the lateral overgrowth is significantly enhanced relative to the axial core growth. We have further examined by XEDS the overgrowth on the bottom (WZ InAs) and upper ( $\text{InAs}_{1-x}\text{Sb}_x$ ) segments for Sb contents up to  $x = 0.25$  (core composition), and find the same trends of higher Sb incorporation in the lateral overgrowth on both the bottom and top segments than in the axial segment. In all cases we also observe that the lateral overgrowth on the WZ bottom segment incorporates somewhat less Sb than the mixed or ZB top segment. These observations extend those reported by Borg *et al* [23] of an increased Sb incorporation in axial  $\text{InAs}_{1-x}\text{Sb}_x$  as compared to the bulk  $\langle 1\bar{1}\bar{1}\rangle_B$  oriented layer. Ternary nanowire surfaces thus behave significantly differently from their 2D layer counterparts, indicating that incorporation is surface crystallographic orientation-dependent. It may therefore also be that incorporation in the lateral overgrowth changes as the facet structure changes, but we were not able to determine that in this study.

### 3.5. The role of antimony

It is interesting to note that not only is the crystal structure of  $\text{InAs}_{1-x}\text{Sb}_x$  nanowires directly related to the composition, but that the entire change of crystal structure from WZ to ZB occurs at very low Sb contents. In other words,

the addition of a rather small amount of Sb to pure InAs changes the crystal structure entirely, with effects observed even for undetectable levels of Sb. By contrast, adding As to InSb does not change the structure until the As level vastly overwhelms the Sb. We might speculate that this relates either to the role of Sb as a surfactant (changing the stable facet structure even for very low concentration), or to the much stronger affinity of Sb in the gold seed particle relative to As (which could dramatically affect the effective V/III ratio at the growth front). We note that, although the entire structure change occurs over a relatively narrow parameter space window, it is not an abrupt change from pure WZ to pure ZB, but rather a tunable change over a range of structural mixtures.

It is well known that the effective V/III ratio can have dramatic consequences for the crystal structure in III–V nanowires [1, 57, 58], as observed by direct tuning of the component sources. In our case, the input amount of Sb in the vacuum is, however, very low compared to the As, and the change in input V/III ratio with the addition of such small amounts of Sb should be negligible. On the other hand, it is also known that the effective V/III ratio in the seed particle is affected by other processes including solubility affinity and diffusivity of the component species in the seed material (in our case gold). Additionally, it is anticipated that the relative solubilities of the various components in the seed alloy are influenced by the others—that is, the concentration of In and/or As in the seed particle may change with the addition of Sb. To understand this further we can compare with the V/III ratio dependence of crystal structure of InAs nanowires grown by MBE. We observe that increasing the V/III ratio either by systematically increasing the As flow, or by periodically pulsing the In flow (to keep it as low as possible), makes it possible to change InAs from nearly pure WZ to twinned ZB (see supplementary figure S10 available at [stacks.iop.org/Nano/23/095702/mmedia](http://stacks.iop.org/Nano/23/095702/mmedia); note that this effect is observable only at relatively large diameters). Based on these observations we speculate that the role of Sb is to increase the total effective V/III ratio at the growth front, very possibly by reducing In surface diffusion or incorporation into the alloy particle.

#### 4. Conclusions

In summary, we have investigated the relationship between structure, facets and composition in ternary  $\text{InAs}_{1-x}\text{Sb}_x$  nanowires using TEM, SEM and STM. We show that the structure of these ternary nanowire materials can be tuned controllably between the pure WZ InAs and ZB InSb phases by varying only the relative group V composition. Specifically, the entire structure change occurs for an Sb content below  $x = 0.15$ , meaning that even a very small addition of Sb to InAs can have dramatic consequences for the crystal phase. Furthermore, we observe that significant conformal lateral overgrowth occurs in parallel with the axial  $\text{InAs}_{1-x}\text{Sb}_x$  nanowire growth, which has an Sb composition notably higher than the axial segment, leading to the formation of core–shell nanowires. In the

case of  $\text{InAs}/\text{InAs}_{1-x}\text{Sb}_x$  single and multiple heterostructure nanowires, the conformal overgrowth is found to behave differently for WZ and ZB segments.

Since the crystal structure of the core nanowire acts as a template for the lateral overgrowth, this gives access to ternary surface facets not accessible in layer systems, including WZ facets. Thanks to an *in situ* As capping technique to protect the facets during transfer, atomically resolved surface structural and quantitative surface compositional information has been obtained for the first time on ZB and WZ ternary nanowire facets. This new technique for nanowire surface protection removes most of the complexity associated with STM studies of nanosurfaces and should now be applicable to a large set of nanostructured materials.

#### Acknowledgments

This work was carried out within IEMN UMR CNRS 8520 and the Nanometer Structure Consortium at Lund University (nmC@LU). We thank G Defoort for his kind contribution in realizing the 3D model and rendering for figure 2(e). T Xu acknowledges financial support from the Direction Générale de l'Armement (DGA) under contract REI-N02008.34.0031. K A Dick acknowledges financial support from nmC@LU, the Swedish Research Council (VR), the Swedish Foundation for Strategic Research (SSF) and the Knut and Alice Wallenberg Foundation (KAW).

#### References

- [1] Caroff P, Bolinsson J and Johansson J 2011 Crystal phases in III–V nanowires: from random toward engineered polytypism *IEEE J. Sel. Top. Quantum Electron.* **17** 829–46
- [2] Thelander C, Caroff P, Plissard S, Dey A W and Dick K A 2011 *Nano Lett.* **11** 2424–9
- [3] Ketterer B, Heiss M, Uccelli E, Arbiol J and Fontcuberta i Morral A 2011 *ACS Nano* **5** 7585–92
- [4] Ikonic Z, Srivastava G P and Inkson J C 1993 *Phys. Rev. B* **48** 17181–93
- [5] Ikonic Z, Srivastava G P and Inkson J C 1994 *Surf. Sci.* **307** 880–4
- [6] Akiyama T, Yamashita T, Nakamura K and Ito T 2011 *Nano Lett.* **10** 4614–8
- [7] Zhang L J, Luo J W, Zunger A, Akopian N, Zwiller V and Harmand J C 2011 *Nano Lett.* **10** 4055–60
- [8] Tsuzuki H, Cesar D F, Rebello de Sousa Dias M, Castelano L K, Lopez-Richard V, Rino J P and Marques G E 2011 *ACS Nano* **5** 5519–25
- [9] Lugani L, Ercolani D, Rossi F, Salviati G, Beltram F and Sorba L 2011 *Cryst. Growth Des.* **10** 4038–42
- [10] Bauer J, Gottschalch V and Wagner G 2008 *J. Appl. Phys.* **104** 114315
- [11] Thelander C *et al* 2010 *Nanotechnology* **21** 205703
- [12] Sköld N, Karlsson L S, Larsson M W, Pistol M-E, Seifert W, Trägårdh J and Samuelson L 2005 *Nano Lett.* **5** 1943–7
- [13] Moore A L, Saha S K, Prasher R S and Shi L 2008 *Appl. Phys. Lett.* **93** 083112
- [14] Sansoz F 2011 *Nano Lett.* **11** 5378–82
- [15] Gil-Santos E, Ramos D, Martinez J, Fernandez-Regulez M, Garcia R, San Paulo A, Calleja M and Tamayo J 2010 *Nature Nanotechnol.* **5** 641–5
- [16] Grantab R and Shenoy V B 2011 *Phil Magn. Lett.* **91** 280–6

- [17] Caroff P, Wagner J B, Dick K A, Nilsson H A, Jeppsson M, Deppert K, Samuelson L, Wallenberg L R and Wernersson L E 2008 *Small* **4** 878–82
- [18] Ercolani D, Rossi F, Li A, Roddaro S, Grillo V, Salviati G, Beltram F and Sorba L 2009 *Nanotechnology* **20** 505605
- [19] Vogel A T, de Boor J, Wittemann J V, Mensah S L, Werner P and Schmidt V 2011 *Cryst. Growth Des.* **11** 1896–900
- [20] Guo Y N, Zou J, Paladugu M, Wang H, Gao Q, Tan H H and Jagadish C 2006 *Appl. Phys. Lett.* **89** 231917
- [21] Jeppsson M, Dick K A, Wagner J B, Caroff P, Deppert K, Samuelson L and Wernersson L-E 2008 *J. Cryst. Growth* **310** 4115–21
- [22] Burke R, Weng X, Kuo M-W, Song Y-W, Itsuno A, Mayer T, Durbin S, Reeves R and Redwing J 2010 *J. Electron. Mater.* **39** 355–64
- [23] Weng X, Burke R A, Dickey E C and Redwing J M 2010 *J. Cryst. Growth* **312** 514–9
- [24] Dheeraj D L, Patriarche G, Zhou H L, Hoang T B, Moses A F, Gronsberg S, van Helvoort A T J, Fimland B O and Weman H 2008 *Nano Lett.* **8** 4459–63
- [25] Plissard S, Dick K A, Wallart X and Caroff P 2010 *Appl. Phys. Lett.* **96** 121901
- [26] Borg B M, Dick K A, Eymery J and Wernersson L E 2011 *Appl. Phys. Lett.* **98** 113104
- [27] Jung C S, Kim H S, Jung G B, Gong K J, Cho Y J, Jang S Y, Kim C H, Lee C-W and Park J 2011 *J. Phys. Chem. C* **115** 7843–50
- [28] Algra R E, Verheijen M A, Borgstrom M T, Feiner L F, Immink G, van Enckevort W J P, Vlieg E and Bakkers E 2008 *Nature* **456** 369–72
- [29] Algra R E et al 2011 *Nano Lett.* **11** 1690–4
- [30] Ganjipour B, Dey A W, Borg B M, Ek M, Pistol M-E, Dick K A, Wernersson L-E and Thelander C 2011 *Nano Lett.* **11** 4222–6
- [31] Voyles P M, Muller D A, Grazul J L, Citrin P H and Gossmann H J L 2002 *Nature* **416** 826–9
- [32] Xu T, Nys J P, Grandidier B, Stievenard D, Coffinier Y, Boukherroub R, Larde R, Cadel E and Pareige P 2008 *J. Vac. Sci. Technol. B* **26** 1960–3
- [33] Berthe M, Stiufluic R, Grandidier B, Deresmes D, Delerue C and Stievenard D 2008 *Science* **319** 436–8
- [34] Mikkelsen A, Skold N, Ouattara L, Borgstrom M, Andersen J N, Samuelson L, Seifert W and Lundgren E 2004 *Nature Mater.* **3** 519–23
- [35] Bolinsson J, Ouattara L, Hofer W A, Skold N, Lundgren E, Gustafsson A and Mikkelsen A 2009 *J. Phys.: Condens. Matter* **21** 055404
- [36] Hilner E, Hakanson U, Froberg L E, Karlsson M, Kratzer P, Lundgren E, Samuelson L and Mikkelsen A 2008 *Nano Lett.* **8** 3978–82
- [37] Neave J H, Joyce B A and Dobson P J 1984 *Appl. Phys. A* **34** 179–84
- [38] Xu T, Nys J P, Addad A, Lebedev O I, Urbietta A, Salhi B, Berthe M, Grandidier B and Stievenard D 2010 *Phys. Rev. B* **81** 115403
- [39] Dubois M, Perdigo L, Delerue C, Allan G, Grandidier B, Deresmes D and Stievenard D 2005 *Phys. Rev. B* **71** 165322
- [40] Soshnikov I P, Cirlin G E, Tonkikh A A, Samsonenko Y B, Dubovskii V G, Ustinov V M, Gorbenko O M, Litvinov D and Gerthsen D 2005 *Phys. Solid State* **47** 2213–8
- [41] Tchernycheva M, Harmand J C, Patriarche G, Travers L and Cirlin G E 2006 *Nanotechnology* **17** 4025–30
- [42] Ihn S-G and Song J-I 2007 *Nanotechnology* **18** 355603
- [43] Tchernycheva M, Travers L, Patriarche G, Glas F, Harmand J-C, Cirlin G E and Dubrovskii V G 2007 *J. Appl. Phys.* **102** 094313
- [44] Plante M C and LaPierre R R 2008 *Nanotechnology* **19** 495603
- [45] Zhou H L, Hoang T B, Dheeraj D L, van Helvoort A T J, Liu L, Harmand J C, Fimland B O and Weman H 2009 *Nanotechnology* **20** 415701
- [46] Shtrikman H, Popovitz-Biro R, Kretinin A, Houben L, Heiblum M, Bukala M, Galicka M, Buczko R and Kacman P 2009 *Nano Lett.* **9** 1506–10
- [47] Plante M C and LaPierre R R 2008 *J. Cryst. Growth* **310** 356–63
- [48] Dick K A, Caroff P, Bolinsson J, Messing M E, Johansson J, Deppert K, Wallenberg L R and Samuelson L 2010 *Semicond. Sci. Technol. B* **25** 024009
- [49] Johansson J, Karlsson L S, Svensson C P T, Martensson T, Wacaser B A, Deppert K, Samuelson L and Seifert W 2006 *Nature Mater.* **5** 574–80
- [50] Caroff P, Dick K A, Johansson J, Messing M E, Deppert K and Samuelson L 2009 *Nature Nanotechnol.* **4** 50–5
- [51] Bolinsson J, Caroff P, Mandl B and Dick K A 2011 *Nanotechnology* **22** 265606
- [52] Ebert P 1999 *Surf. Sci. Rep.* **33** 121–303
- [53] Steinshneider J, Harper J, Weimer M, Lin C H, Pei S S and Chow D H 2000 *Phys. Rev. Lett.* **85** 4562–5
- [54] Zuo S L, Hong Y G, Yu E T and Klem J F 2002 *J. Appl. Phys.* **92** 3761–70
- [55] Gomya A, Ohkouchi S and Kawamura Y 2007 *J. Cryst. Growth* **301** 47–9
- [56] Timm R, Eisele H, Lenz A, Ivanova L, Balakrishnan G, Huffaker D L and Daehne M 2008 *Phys. Rev. Lett.* **101** 256101
- [57] Paiman S et al 2009 *Nanotechnology* **20** 225606
- [58] Joyce H J, Wong-Leung J, Gao Q, Tan H H and Jagadish C 2010 *Nano Lett.* **10** 908–15